ORIGINAL PAPER

Solvothermal synthesis of TiNb$_2$O$_7$ microspheres as anodic materials for high-performance lithium–ion batteries

Wenkui Zhang[1] · Jian Bao[1] · Chengwei Lu[1] · Xiaozheng Zhou[1] · Xinhui Xia[1] · Jun Zhang[1] · Xinping He[1] · Yongping Gan[1] · Hui Huang[1] · Chen Wang[1,2] · Wangjun Wan[2] · Ruyi Fang[1] · Yang Xia[1]

Abstract

TiNb$_2$O$_7$ (TNO) has been regarded as a promising anode material for high-power lithium–ion batteries due to its high theoretical capacity and work voltage (387.6 mA h g^{-1}, 1.6 V vs. Li$^+$/Li). Herein, a series of microspherical TNO anode materials are synthesized by a facile solvothermal method, and the effect of solvothermal time on the microstructure and electrochemical performance is investigated. Specifically, when the solvothermal time is 12 h, the TNO microsphere (TNO-12) exhibits higher specific surface area and more reasonable pore size distribution. As a result, TNO-12 anode delivers a high reversible discharge capacity of 299.87 mA h g^{-1} with a superior initial coulombic efficiency above 98.5%, excellent cycling capacity retention of 80.15% after 100 cycles at 0.5 C (150 mA g^{-1}), and good rate performance at 0.1–2 C. Most importantly, the full cell constructed with TNO anode and commercial oxide cathode (LiNi$_{0.6}$Mn$_{0.4}$O$_2$/LiMn$_2$O$_4$ with a mass ratio of 85 : 15) exhibits excellent cycling stability at high current densities (79.14% after 100 cycles at 0.5 C). This study optimizes the synthesis process for high-performance microspherical TNOs, providing new insights for the next generation of commercial anodes.

Keywords TiNb$_2$O$_7$ · Titanium-based oxide · Solvothermal · Li-ion full batteries

Introduction

The expanding electric vehicle industry has led to a strong demand growth of lithium–ion batteries [1–6]. In this regard, the key determinant of their electrochemical performance is electrode materials [7–12]. Graphite anode has dominated the market since its first commercialization. As a typical intercalation-type anode material, the layered structure of graphite has good structural stability during intercalation/deintercalation of lithium–ion (6 C + xLi$^+$ + xe$^-$ ↔ Li$_x$C$_6$). However, due to its low operating potential (0.1 V *vs.* Li$^+$/Li), it is prone to lithium dendrite during cycling, leading to internal short circuits in the battery, which can cause serious safety problems [13]. In addition, the decomposition of the electrolyte and the formation of a solid electrolyte interface (SEI) film on the material surface at lower operating potentials will greatly affect the initial Coulombic efficiency of the battery.

To overcome the challenges inherent in low operating voltage anode materials, identifying an innovative high-voltage, high-performance anode material is an immediate priority. The most widely investigated of all is Li$_4$Ti$_5$O$_{12}$ (denoted as LTO), which has an average voltage of 1.55 V and a capacity of about 150 mA h g^{-1} [14–16]. Compared to the 0.10 V of standard graphite anode, although the average lithiation potential of 1.55 V reduces the energy density of the full battery, it is still advantageous due to its resistance to dendrite formation and the hindrance of solid electrolyte interphase (SEI) formation, even at high current densities [17–19]. In addition, TiNb$_2$O$_7$ (denoted as TNO) is another anode material with high lithiation potential in great demand [20]. Due to five lithium atoms being insertable into the layered structure with three redox pairs (Nb^{5+}/Nb^{4+}, Nb^{4+}/Nb^{3+}, Ti^{4+}/Ti^{3+}), the theoretical capacity of TNO is almost double that of LTO anode at approximately 387 mA h g^{-1}.

✉ Ruyi Fang
1112101045@zjut.edu.cn

✉ Yang Xia
nanoshine@zjut.edu.cn

1 College of Materials Science and Engineering, Zhejiang University of Technology, Hangzhou 310014, China

2 Zhejiang Academy of Science and Technology for Inspection & Quarantine, Hangzhou 311215, China

This makes TNO a better candidate to substitute graphite as anode material than LTO in the future [21–24].

The structural characteristics of electrode materials significantly affect their electrochemical performance. As a result, it is crucial to employ appropriate synthesis parameters and processes to achieve the desired morphology, size, phase, and composition. The high-temperature solid phase method is a popular choice as it is simple, cost-effective, and easy to operate. It is widely used for the synthesis of granular TNO. Choi et al. synthesized TNO by solid phase method by using TiO_2 and Nb_2O_5 as raw materials [25]. However, non-uniform composition, agglomeration of particles, and large particle size are the disadvantages of the synthesized products. For nanoscale products, the sol–gel method is preferred [26], which was employed by Ise et al. for synthesizing TNO nanoparticles (ranging from 50 to 300 nm) using $NbCl_5$ and $TiOSO_4$. However, the sol–gel method has the drawback of a lengthy synthesis cycle and the generation of gas during drying [27]. The solvothermal method is another option that can produce nanoparticles with better dissolution, dispersion, and reaction activity [28]. Li et al. synthesized TNO microspheres with a three-dimensional nanopore structure by the solvothermal method, and the particle size of products is 2–3 μm [29]. The study findings demonstrate diverse forms of TNO morphologies, including spherical, one-dimensional (1D), three-dimensional (3D) porous, and particulate shapes, which can be achieved via distinct synthetic approaches. While size and porosity are among the factors influencing the Li–ion storing capacity of TNO, the research suggests that the spherical morphology exhibits superior electrochemical performance in comparison to others. Typically, spherical TNO is generally prepared by the solvothermal method.

In line with these advances, we prepared TNO microspheres with high specific surface area and reasonable pore size distribution using solvothermal method as promising alternatives to develop commercial anode material for high-performance lithium–ion full batteries. The effect of solvothermal time on TNO was explored in focus. The phase composition and microstructure of the TNO microspheres are systematically studied. Meanwhile, the electrochemical performance is comprehensively evaluated by charge–discharge test, cyclic voltammetry, and electrochemical impedance spectroscopy. Remarkably, TNO microspheres prepared at solvothermal time of 12 h (TNO-12) show cleanest and densest microsphere morphology, as well as a higher specific surface area and the most favorable pore size distribution compared to other samples. This optimal morphological structure of TNO leads to a high specific capacity, long cycling lifespan, and enhanced rate capability. In addition, blending two or more active materials (i.e., creating physical mixtures) is a widely used strategy in commercial batteries to achieve better performance compared to a single component. Therefore, the full cell constructed with TNO anode and $LiNi_{0.6}Mn_{0.4}O_2/LiMn_2O_4$ blended cathode is assembled and exhibits excellent cycling stability at high current densities. This work offers a new reach direction for the design and synthesis of high work voltage anode for high-performance lithium–ion full batteries.

Experimental

Material preparation

$NbCl_5$ (Shanghai Aladdin Biochemical Technology Co., Ltd.) and tetrabutyl titanate (Shanghai Aladdin Biochemical Technology Co., Ltd.) were used as Nb drinkable and Ti precursors, respectively, to synthesize $TiNb_2O_7$ powders using solvothermal. Specifically, a mixture of tetrabutyl titanate and $NbCl_5$ in a 1:2 ratio was added to 40 ml of ethanol (99%, Aladdin) and mixed at room temperature for 20 min. The resulting mixture was then transferred to a Teflon-lined autoclave and subjected to solvothermal treatment at 180 °C for 8, 12, and 16 h, respectively. The resulting precipitates were washed multiple times with deionized water, and the obtained powders, referred to as TNO precursors, were calcined at 900 °C for 6 h in the presence of air using a muffle furnace. The samples were abbreviated as TNO-X, where X represents the solvothermal time.

$LiNi_{0.6}Mn_{0.4}O_2$ (denoted as NM64, Zhejiang Hitrans Lithium Battery Technology Co. Ltd.) and $LiMn_2O_4$ (denoted as LMO, Zhejiang Hitrans Lithium Battery Technology Co. Ltd.) were mixed thoroughly to form blended cathode materials (simple mechanical mixing) with mass ratios of 85:15 marked as 15NM.

Material characterizations

The TNO anode materials prepared with different solvothermal times were characterized via X-ray diffraction (XRD, PANalytical X'Pert Pro) with Cu Kα radiation ($\lambda = 0.1541$ nm) in the 2θ range of 10–60°. The morphology of TNO and TNO precursors observed by scanning electron microscope (SEM, FEI Nova NanoSEM450). The specific surface area and pore size distribution of the samples were calculated by the Brunauer–Emmett–Teller (BET) method and the nonlocal density functional theory (NLDFT) method, respectively.

Cell assembly and electrochemical measurements

For half-cell tests of the TNO, 2025-type coin cells were used with metallic Li foils as the anodes. The active electrode slurry contained 80 $wt\%$ active material, 10 $wt\%$

conductive additive (Super-P), and 10 *wt%* polyvinylidene fluoride (PVDF) in N-methyl-2-pyrrolidone (NMP), and the solid content was 28%. After the slurry was coated on the copper foil, the working electrode was placed in an air-circulating oven at 80 °C for 2 h and then transferred to vacuum oven at 120 °C for 10 h. The electrolyte was 1 M $LiPF_6$ in a 1:1:1 ratio of ethylene carbonate (EC), dimethyl carbonate (DEC), and ethyl methyl carbonate (EMC).

For the full-cell tests, the blended material (15NM) and TNO were used as the cathode and anode materials, respectively. Electrochemical experiments were conducted by CR2032-type coin cells. The cathode slurry was composed of active material, conductive additive (Super-P), and polyvinylidene fluoride (PVDF) binder by a mass ratio of 85:8:7. The solvent was N-methyl-2-pyrrolidone (NMP), and the solid content was 28%. After the slurry was coated on the aluminum foil, the cathode was placed in an air-circulating oven at 80 °C for 2 h and then transferred to vacuum oven at 120 °C for 10 h. The anode preparation process is the same as for the above-mentioned half-cells. A Celgard 2300 membrane was employed to separate cathode and anode. The electrolyte was 1 M $LiPF_6$ in a 1:1:1 ratio of ethylene carbonate (EC), dimethyl carbonate (DEC), and ethyl methyl carbonate (EMC). The specific structure of the full cell is illustrated in Fig. S1.

Cyclic voltammogram (CV) was measured on an Ivium multichannel potentiostatic-galvanostatic system at a scan rate of 0.1 mV s^{-1}. The electrochemical impedance spectra (EIS) were obtained using a CHI650B electrochemical workstation (Chenhua in Shanghai, China), over a frequency range of 1 to 10^6 Hz and an amplitude of 5 mV. The cells were tested at constant rate of 0.2 C (1 C = 180 mA g^{-1}) within the potential range of 2.5 ~ 4.2 V by a battery test system (Neware Technology Co., Ltd.).

Results and discussion

Material characterization

To investigate the effect of solvothermal time on the product morphology, SEM images of the TNO precursors and TNO materials are presented in (Figs. S2, 1). The panoramic morphologies of the TNO precursors and TNO samples at low magnification show monodisperse and microsphere structure with the particle size of 2 to 6 μm. The surface of TNO-8 precursors is smooth and clean, while the surfaces of TNO-12 and TNO-16 precursors show obvious granularity. Upon calcination, TNO-8 material has irregular primary particle composition with loose structure. Although the structures of both TNO-12 material and TNO-16 material are extremely dense, excess micro particles are generated on the surface of TNO-16 microspheres as shown in the red circle in Fig. 1c. This microstructure of TNO-12 possesses thermal stability, which can prevent structural collapse during electrochemical cycling. At the same time, the TNO-12 microsphere is composed of many highly uniform nano primary particles, giving it high porosity, which is conducive to the permeation of the electrolyte [29].

As shown in Fig. 2a, the high crystallinity and phase purity of the as-prepared TNO microspheres are confirmed and the diffraction peak of all samples corresponds well to the standard card of $TiNb_2O_7$ (PDF#39–1407), indicating a typical layered ReO_3 structure. There are no other secondary or parasitic phase peaks detected, such as TiO_2, Nb_2O_5, or $Ti_2Nb_{10}O_{29}$, which reveals the high purity of the product [30, 31]. Additionally, nitrogen adsorption isotherms and pore size distribution of TNO microspheres prepared at different solvothermal times are displayed in Fig. 2b and c. All the isotherms are similar to type III isotherms, and the curves are concave downward throughout the interval of relative pressure with no inflection points.

Fig. 1 SEM images of TNO at different magnifications: **a** TNO-8 h, **b** TNO-12 h, and **c** TNO-16 h, respectively
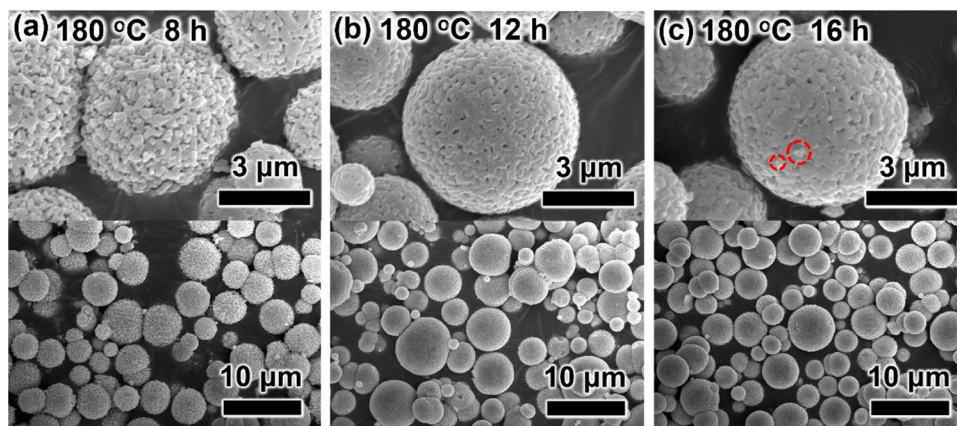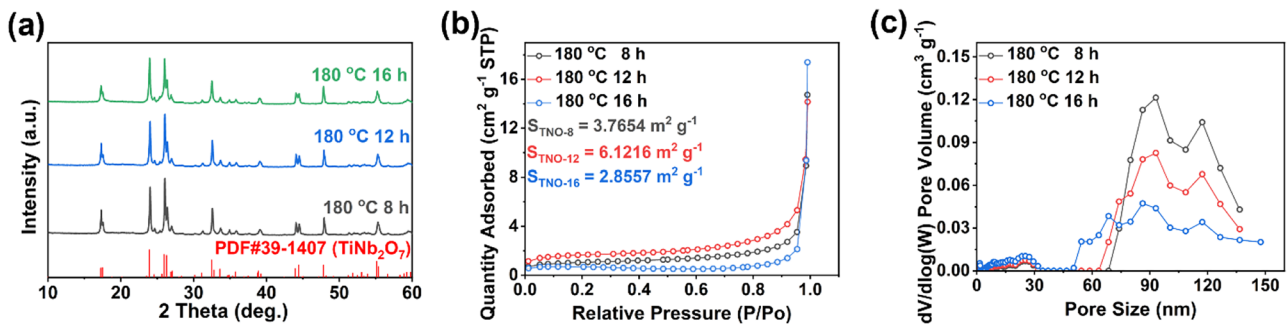
Fig. 2 **a** XRD patterns, **b** nitrogen adsorption isotherms, and **c** pore size distribution of TNO at different solvothermal times

It is due to the fact that the interaction between nitrogen molecules is stronger than that between nitrogen and sample. The BET surface area of TNO-12 is calculated to be the largest (6.12 m^2 g^{-1}), compared with only 3.77 m^2 g^{-1} and 2.86 m^2 g^{-1} for TNO-8 and TNO-16. Further analysis of the pore size distribution of the materials reveals that all samples have a broad pore sizes distribution ranging from 4 to 120 nm. The pore sizes are mainly distributed between 70 and 120 nm which makes them macroporous materials. For TNO-8, the maximum number of macropores is determined by its loose structure, which affects the structural stability, and TNO-16 has the minimum number of macropores, which limits the permeation of the electrolyte, causing low utilization of active material.

Electrochemical properties

To determine the optimal reaction time, CR2025 coin cells were assembled to evaluate the electrochemical performance of various TNO samples. Figure 3a-c shows the CV curves of TNO electrodes prepared at different solvothermal times. Apparently, the CV characteristics are in general agreement with other structures of TNO electrodes prepared by different methods recorded in the publication [32–34]. Unlike other research reported that there is one pair of peaks in range of 1.69–1.93 V caused by different titanium states in TNO, these redox peaks are not apparent in TNO microspheres. The appearance of peaks located at 1.50 V and 1.75 V can be attributed to the Nb^{5+}/Nb^{4+} redox couples.

Fig. 3 The CV profiles obtained at the scan rate of 0.1 mV s^{-1}: **a** TNO-8 h, **b** TNO-12 h, and **c** TNO-16 h, respectively. **d** Electrochemical impedance spectroscopy, the inset is the corresponding equivalent circuit
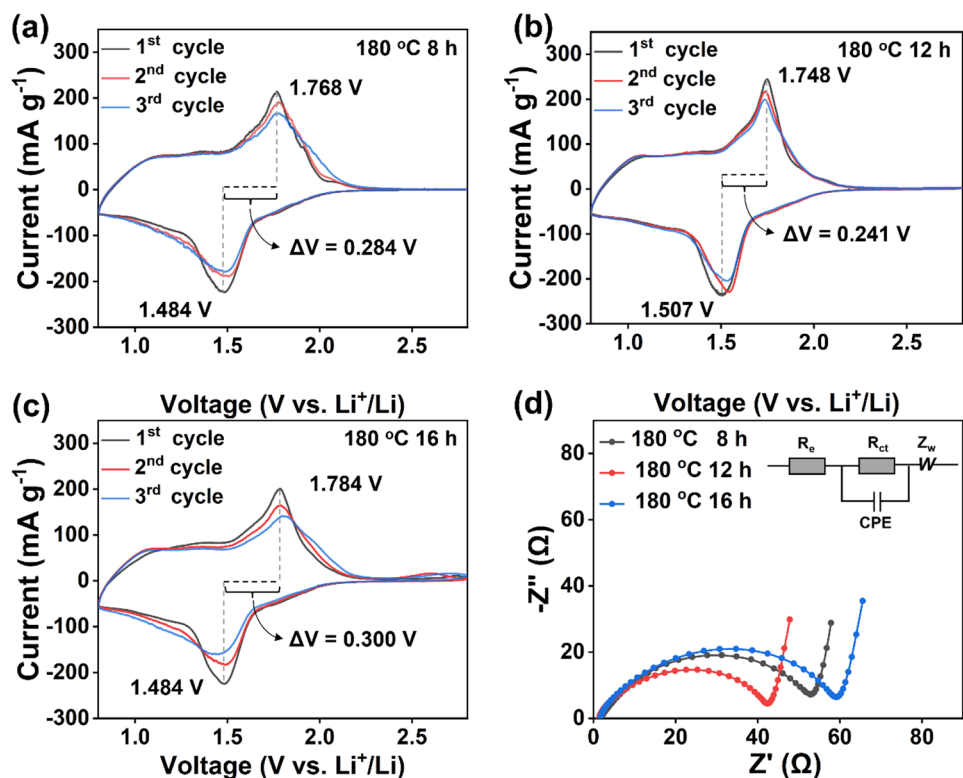
The broad bump in the range of 1.0–1.4 V may correspond to the Nb^{4+}/Nb^{3+} redox couples [29]. The highest overlap of CV curves is observed for the TNO-12 electrode compared to the TNO-8 and TNO-16 electrodes, with the smallest potential difference between the redox peaks of Nb^{5+}/Nb^{4+} and the lowest peak potential of the first oxidation peak. It suggests superb cyclability and excellent kinetics of TNO-12 electrode. Electrochemical impedance spectroscopies of different solvothermal times are illustrated in Fig. 3d. It is clear that the TNO-12 shows the smallest charge transfer resistance (R_{ct}) [35].

Figure 4a-c illustrates the charge–discharge curves of TNO-8, TNO-12, and TNO-16 electrodes at initial three cycles. The shape of the charge/discharge curves are the same for all electrodes and the voltage curves shows sloping lines during both charge and discharge processes. It can be also seen that the discharge plateaus of the TNO electrodes near 1.65 V correspond to the redox peak at 1.75/1.50 V. Moreover, the initial lithiation (discharge) capacity of TNO-8, TNO-12, and TNO-16 is 283.36, 299.87, and 291.30 mA h g^{-1}, respectively. Obviously, the TNO microspheres prepared with a solvothermal time of 12 h provides the maximum discharge capacity. Moreover, the initial columbic efficiency value of all electrodes is above 98.5%, indicating the low irreversible reactions, which is benefited from the high work voltage of the TNO electrode without

solid electrolyte interface (SEI) generation in the first cycle. Therefore, it is superior to adopt TNO as the anode for the full cell.

The long-term cycling ability of the TNO electrodes at a current density of 150 mA g^{-1} is presented in Fig. 4d. The similar capacity reduction upon early cycling is observed for all three electrodes. After 60 cycles, the discharge capacity of TNO-8 electrode dropped sharply. Meanwhile, 180–12 electrode shares the same downward trend as 180–16 electrode, except that the reversible capacity of 180–16 electrode is lower. The capacity retentions of TNO-8, TNO-12, and TNO-16 electrodes after 100 cycles are 70.47%, 80.15%, and 74.97%, respectively. Additionally, the rate capability of the TNO electrodes prepared at different solvothermal times is verified by multi-rate tests. As displayed in Fig. 4e, the TNO prepared with a solvothermal time of 12 h show excellent rate performance, which are far superior than that of TNO-8 electrode. Even at a high current density of 2.0 C, TNO-12 electrode still has a high reversible capacity of 238.80 mA h g^{-1}, whereas the TNO-8 electrode only delivers 185.33 mA h g^{-1}. Noticeably, when the current density gradually decreases, 180–12 and 180–16 electrodes both recover high reversible capacity.

Figure 5 demonstrates the SEM images of various TNO electrodes obtained at different solvothermal times after 100 cycles. Apparently, all TNO samples maintain their
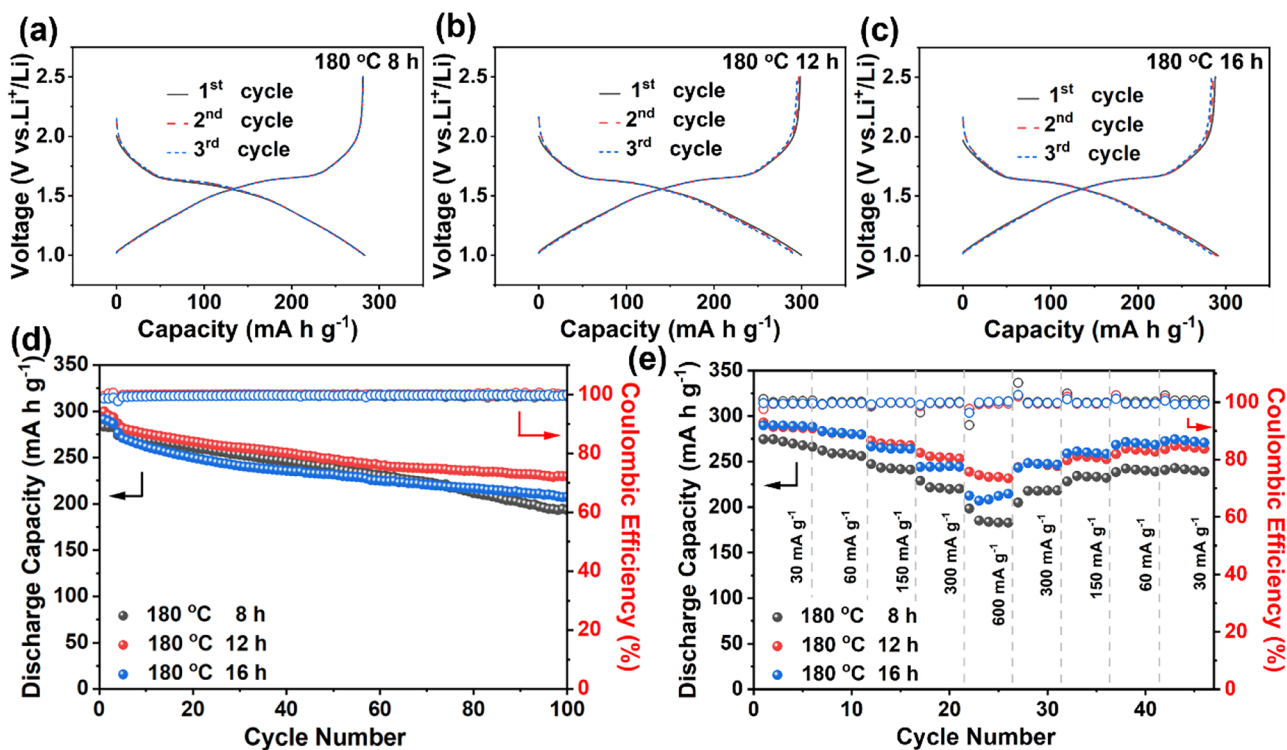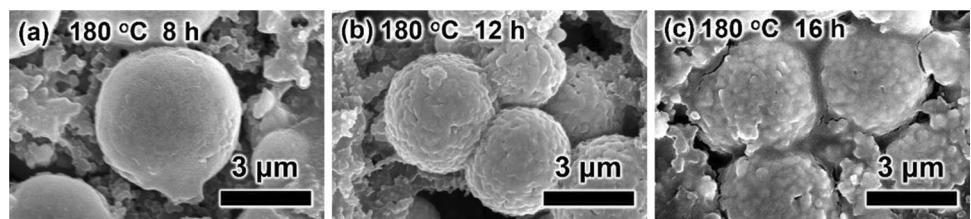

Fig. 4 Charge–discharge curves of the initial three cycles: **a** TNO-8, **b** TNO-12, and **c** TNO-16. **d** Cycling performance and **e** rate performance of TNO prepared at different solvothermal times

(a) 180 °C 8 h   (b) 180 °C 12 h   (c) 180 °C 16 h   3 µm

original intact spherical structure after 100 cycles, showing the excellent structural stability of the TNO microspheres. On the other hand, according to a widely accepted view, the electrolyte decomposition and SEI film formation occur only near 0.8 V [36]. Therefore, TNO exhibits high intercalation potential of about 1.65 V *vs.* Li^+/Li, which is traditionally believed to avoid the electrolyte decomposition and effectively inhibit the formation of SEI film [37–39]. However, in the actual operation process, a thick layer of SEI film can be clearly observed on the surface of TNO-8 and TNO-16. It significantly increases the interfacial impedance between the electrode and electrolyte and consumes the active lithium ions, consequently affecting the cycling stability of the electrode. In contrast, the SEI film of TNO-12 is thin and uniform, which can prevent further reduction reaction between electrolyte and electrode during the cycling.

To stand out the practical application feasibility of TNO in Li–ion batteries, 15NM-TNO full cells are assembled to further evaluation the electrochemical performance. In Fig. S3, the capacity retention rates of full cells with N/P ratios of 1.1:1, 1.05:1, 1:1, and 0.95:1 for 60 cycles are 75.80%, 92.95%, 82.92%, and 74.42%, respectively. Obviously, 1.05:1 proved to be the best NP ratio for assembling full cells. Figure 6a shows the impedance plot of the full cell, which shows that the bulk impedance R_e of the full cell is about 2.5 Ω and the charge transfer impedance R_{ct} is about 25 Ω, both within the ideal range [35, 40, 41]. Figure 6b shows the charge/discharge graph of the full cell; the discharge plateau of the full cell is around 2.1 V, which is determined by the difference between the discharge plateau of the cathode material (3.8 V) and the discharge plateau of the anode material (1.7 V). To reveal the stability of the full cell, differential capacity curve was presented in Fig. 6c.
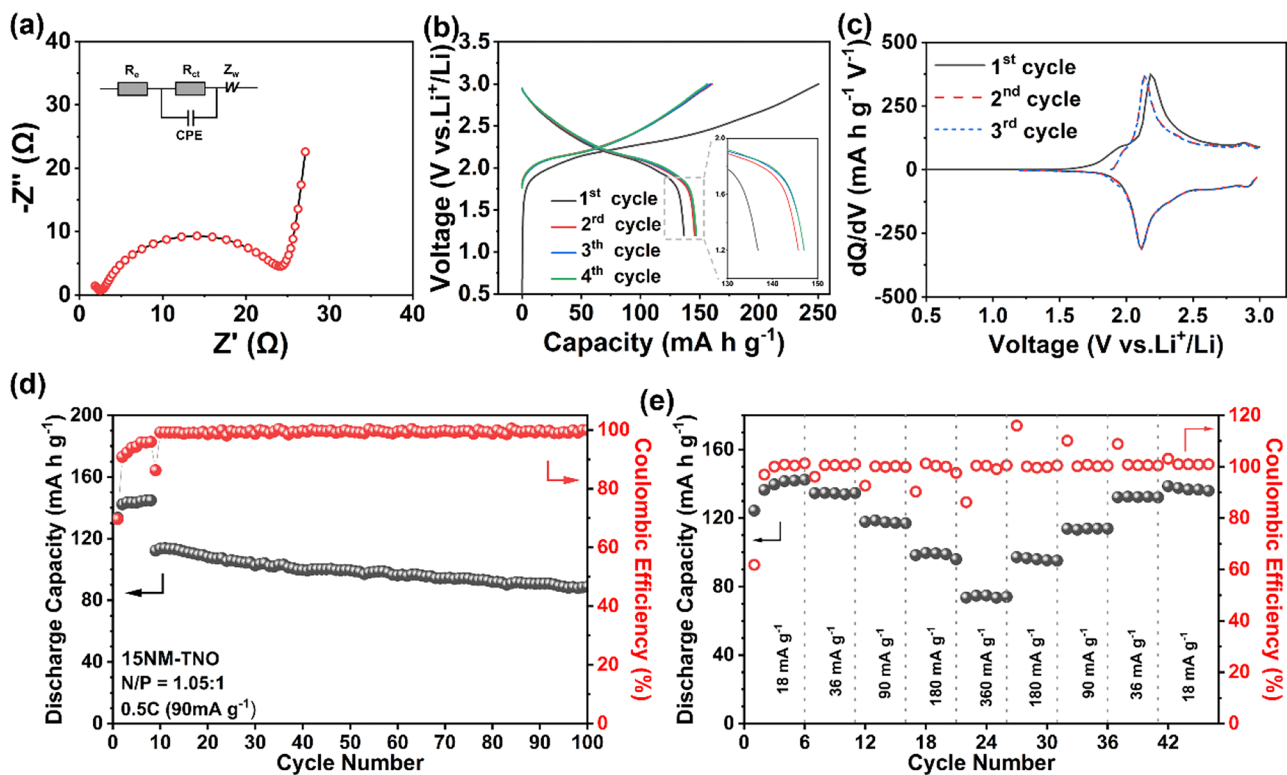

Fig. 6 **a** Electrochemical impedance spectroscopy of full cell before cycling. **b** Charge–discharge curves for the initial four cycles. **c** dQ dV^{-1} curves for the initial three cycles. **d** Cycling performance and **e** rate performance of full cell with N/P ratio of 1.05:1

After the first cycle, the horizontal coordinate of the peak corresponding to the charge is shifted. The second and third cycle differential capacity curves coincide closely, indicating that the full-cell system possesses good charge/discharge reversibility. In addition, Fig. 6d shows the discharge capacity of the full cell at a high current density of 0.5 C (90 mA g^{-1}). The Coulombic efficiency of the first cycle of the full battery is about 69.65%. During the activation phase of the battery (the initial eight cycles), the discharge capacity is increasing, after the end of the activation procedure, the Coulombic efficiency of the battery remains stable (> 99%), and it has good cycling stability. To be more specific, the full cell delivers the acceptable initial discharge capacities of 112.24 mA h g^{-1} at 0.5 C. After 100 cycles, the reversible capacities are 88.83 mA h g^{-1} with satisfactory capacity retentions of 79.14% at 0.5 C. Figure 6e presents the multi-rate capability comparison of full cell. Impressively, the cell delivers remarkable specific discharge capacities of 141.56, 134.49, 117.61, 99.38, and 74.84 mA h g^{-1} at 0.1, 0.2, 0.5, 1.0, and 2.0 C, respectively, along with a high and stable Coulombic efficiency above 99%. Subsequently, the reversible capacity of the cell rose back to 136.65 mA h g^{-1} when the current density returned to 0.1 C. It shows that the full-cell system has good stability and rate performance.

In short, optimizing the preparation process to improve the morphological structure of TNO anode is necessary for enhancing its performance. Due to the higher specific surface area and reasonable pore size distribution, the TNO-12 anode shows a high energy density, long cycle life, and excellent rate performance. In addition, the excellent electrochemical performance of full battery also paves the way for its future practical application.

Conclusions

In summary, a series of microspherical TNO anode materials are synthesized by facile solvothermal method. The TNO microsphere prepared at solvothermal time of 12 h (TNO-12) shows the cleanest and densest microsphere morphology. Meanwhile, the higher specific surface area and the most favorable pore size distribution of TNO-12 make it more conducive to the diffusion of Li$^+$. As a result, TNO-12 exhibits a high specific discharge capacity, excellent cycling performance, and rate performance. More importantly, the full cell constructed with TNO anode and NM64 cathode also demonstrates excellent cycling stability at high current densities. We expect this work to promote the practical implementation of lithium–ion batteries with high energy density.

Authors' contributions Wenkui Zhang: writing—original draft and funding acquisition. Jian Bao: investigation, data curation, and writing—original draft. Chengwei Lu: investigation and data curation. Xiaozheng Zhou: formal analysis and data curation. Xinhui Xia: formal analysis and data curation. Jun Zhang: investigation and formal analysis. Xinping He: investigation and visualization. Yongping Gan: formal analysis and visualization. Hui Huang: formal analysis and data curation. Chen Wang: formal analysis and visualization. Wangjun Wan: formal analysis and data curation. Ruyi Fang: supervision and writing—review and editing. Yang Xia: supervision, funding acquisition, and conceptualization.

Declarations

Conflict of interests The authors declare no competing interests.

References

1. Yang X-G, Liu T, Wang C-Y (2021) Thermally modulated lithium iron phosphate batteries for mass-market electric vehicles. Nat Energy 6:176–185. https://doi.org/10.1038/s41560-020-00757-7
2. Liu Y-N, Xiao Z, Zhang W-K, Zhang J, Huang H, Gan Y-P, He X-P, Kumar GG, Xia Y (2022) Poly(m-phenylene isophthalamide)-reinforced polyethylene oxide composite electrolyte with high mechanical strength and thermostability for all-solid-state lithium metal batteries. Rare Met 41:3762–3773. https://doi.org/10.1007/s12598-022-02065-3
3. Su H, Liu Y, Zhong Y, Li J, Wang X, Xia X, Gu C, Tu J (2022) Stabilizing the interphase between Li and Argyrodite electrolyte through synergistic phosphating process for all-solid-state lithium batteries. Nano Energy 96:107104. https://doi.org/10.1016/j.nanoen.2022.107104
4. Liu P, Su H, Liu Y, Zhong Y, Xian C, Zhang Y, Wang X, Xia X, Tu J (2022) LiBr–LiF-rich solid–electrolyte interface layer on lithiophilic 3D framework for enhanced lithium metal anode. Small Struct 3:2200010. https://doi.org/10.1002/sstr.202200010
5. Wang J, Wang Z, Ni J, Li L (2022) Electrospun materials for batteries moving beyond lithium-ion technologies. Electrochem Energy Rev 5:211–241. https://doi.org/10.1007/s41918-021-00103-9
6. Jiang Y, Wang Y, Ni J, Li L (2021) Molybdenum-based materials for sodium-ion batteries Infomat 3:339–352. https://doi.org/10.1002/inf2.12175
7. Chen AQ, Wang K, Li JJ, Mao QZ, Xiao Z, Zhu DM, Wang GG, Liao P, He JR, You Y, Xia Y (2020) The formation, detriment and solution of residual lithium compounds on Ni-rich layered oxides in lithium-ion batteries. Front Energy Res 8:593009. https://doi.org/10.3389/fenrg.2020.593009
8. Xia Y, Chen AQ, Wang K, Mao QZ, Huang H, Zhang J, He XP, Gan YP, Xiao Z, Zhang WK (2022) Industrial modification comparison of Ni-Rich cathode materials towards enhanced surface chemical stability against ambient air for advanced lithium-ion batteries. Chem Eng J 450:138382. https://doi.org/10.1016/j.cej.2022.138382

9. Xia Y, Ren XH, Xiao Z, Gan YP, Zhang J, Huang H, He XP, Mao QZ, Wang GG, Zhang WK (2022) Spinel $LiNi_{0.5}Mn_{1.5}O_4$ shell enables Ni-rich layered oxide cathode with improved cycling stability and rate capability for high-energy lithium-ion batteries. Electrochimica Acta 418:140352. https://doi.org/10.1016/j.electacta.2022.140352

10. Jiao C, Qiuying X, Wei L, Hui X (2022) Enhancing the lithium storage capability of TiO_2 thin film for all-solid-state microbatteries via amorphous-crystalline heterostructure design. Appl Phys Lett 121:131901. https://doi.org/10.1063/5.0117083

11. Zhu S, Sheng J, Ni J, Li Y (2021) 3D vertical arrays of nanomaterials for microscaled energy storage devices. Acc Mater Res 2:1215–1226. https://doi.org/10.1021/accountsmr.1c00175

12. Zhang Y, Zhang Q, Wang J, Sheng L, Wang L, Xie Y, Hao Y, Dong L, He X (2022) Insight mechanism of nano iron difluoride cathode material for high-energy lithium-ion batteries: a review. J Solid State Electrochem 26:2601–2626. https://doi.org/10.1007/s10008-022-05287-8

13. Reddy MV, Subba Rao GV, Chowdari BVR (2013) Metal oxides and oxysalts as anode materials for Li ion batteries. Chem Rev 113:5364–5457. https://doi.org/10.1021/cr3001884

14. Thackeray MM, Amine K (2021) $Li_4Ti_5O_{12}$ spinel anodes. Nat Energy 6:683–683. https://doi.org/10.1038/s41560-021-00829-2

15. Verde MG, Baggetto L, Balke N, Veith GM, Seo JK, Wang Z, Meng YS (2016) Elucidating the phase transformation of $Li_4Ti_5O_{12}$ lithiation at the nanoscale. ACS Nano 10:4312–4321. https://doi.org/10.1021/acsnano.5b07875

16. Yuan T, Tan Z, Ma C, Yang J, Ma Z-F, Zheng S (2017) Challenges of spinel $Li_4Ti_5O_{12}$ for lithium-ion battery industrial applications. Adv Energy Mater 7:1601625. https://doi.org/10.1002/aenm.201601625

17. Tang Y, Deng S, Shi S, Wu L, Wang G, Pan G, Lin S, Xia X (2020) Ultrafast and durable lithium storage enabled by intertwined carbon nanofiber/$Ti_2Nb_{10}O_{29}$ core-shell arrays. Electrochimica Acta 332:135433. https://doi.org/10.1016/j.electacta.2019.135433

18. Shen S, Zhang S, Deng S, Pan G, Wang Y, Liu Q, Wang X, Xia X, Tu J (2019) Bioinspired large-scale production of multidimensional high-rate anodes for both liquid & solid-state lithium ion batteries. J Mater Chem A 7:22958–22966. https://doi.org/10.1039/C9TA08899G

19. Deng S, Zhang Y, Xie D, Yang L, Wang G, Zheng X, Zhu J, Wang X, Yu Y, Pan G, Xia X, Tu J (2019) Oxygen vacancy modulated $Ti_2Nb_{10}O_{29-x}$ embedded onto porous bacterial cellulose carbon for highly efficient lithium ion storage. Nano Energy 58:355–364. https://doi.org/10.1016/j.nanoen.2019.01.051

20. Chen J, Ni M, Liu W, Xia Q, Xia H (2022) N-doped carbon-coated interconnected $TiNb_2O_7$ hollow nanospheres as advanced anodes for lithium-ion batteries. J Mater Sci 57:15502–15512. https://doi.org/10.1007/s10853-022-07610-0

21. Muruganantham R, Lin M-C, Wang PK, Chang BK, Liu W-R (2022) Highly effective Al-doped titanium niobate porous anode material for rechargeable high-rate Li-ion storage performance. J Taiwan Inst Chem Eng 131:104187. https://doi.org/10.1016/j.jtice.2021.104187

22. Aghamohammadi H; Eslami-Farsani R (2022) Effects of calcination parameters on the purity, morphology, and electrochemical properties of the synthesized $TiNb_2O_7$ by the solvothermal method as anode materials for Li-ion batteries. J Electroanalytical Chem 917:116394. https://doi.org/10.1016/j.jelechem.2022.116394

23. Zhang Y, Kang C, Zhao W, Sun B, Xiao X, Huo H, Ma Y, Zuo P, Lou S, Yin G (2022) Crystallographic engineering to reduce diffusion barrier for enhanced intercalation pseudocapacitance of $TiNb_2O_7$ in fast-charging batteries. Energy Storage Mater 47:178–186. https://doi.org/10.1016/j.ensm.2022.01.061

24. Shen S, Guo W, Xie D, Wang Y, Deng S, Zhong Y, Wang X, Xia X, Tu J (2018) A synergistic vertical graphene skeleton and S-C shell to construct high-performance $TiNb_2O_7$-based core/shell arrays. J Mater Chem A 6:20195–20204. https://doi.org/10.1039/C8TA06858E

25. Choi SH, Ali B, Choi KS, Hyun SK, Sim JJ, Choi WJ, Joo W, Lim JH, Lee TH, Kim TS, Park KT (2017) Reaction kinetics and morphological study of $TiNb_2O_7$ synthesized by solid-state reaction. Arch Metall Mater 2B:1051–1056. https://doi.org/10.1515/amm-2017-0152

26. Lu C-H, Li K-C, Balaji S, Kumar PS (2021) Agar-assisted sol-gel synthesis and electrochemical characterization of $TiNb_2O_7$ anode materials for lithium-ion batteries. Ceram Int 47:18619–18624. https://doi.org/10.1016/j.ceramint.2021.03.193

27. Ise K, Morimoto S, Harada Y, Takami N (2018) Large lithium storage in highly crystalline $TiNb_2O_7$ nanoparticles synthesized by a hydrothermal method as anodes for lithium-ion batteries. Solid State Ionics 320:7–15. https://doi.org/10.1016/j.ssi.2018.02.027

28. Cheng Q, Liang J, Lin N, Guo C, Zhu Y, Qian Y (2015) Porous $TiNb_2O_7$ Nanospheres as ultra long-life and high-power anodes for lithium-ion batteries. Electrochim Acta 176:456–462. https://doi.org/10.1016/j.electacta.2015.07.038

29. Li H, Shen L, Pang G, Fang S, Luo H, Yang K, Zhang X (2015) $TiNb_2O_7$ nanoparticles assembled into hierarchical microspheres as high-rate capability and long-cycle-life anode materials for lithium ion batteries. Nanoscale 7:619–624. https://doi.org/10.1039/C4NR04847D

30. Wu X, Miao J, Han W, Hu Y-S, Chen D, Lee J-S, Kim J, Chen L (2012) Investigation on $Ti_2Nb_{10}O_{29}$ anode material for lithium-ion batteries. Electrochem Commun 25:39–42. https://doi.org/10.1016/j.elecom.2012.09.015

31. Li H, Shen L, Zhang X, Nie P, Chen L, Xu K (2012) Electrospun hierarchical $Li_4Ti_{4.95}Nb_{0.05}O_{12}$/carbon composite nanofibers for high rate lithium ion batteries. J Electrochem Soc159:A426. https://doi.org/10.1149/2.066204jes

32. Wang H, Qian R, Cheng Y, Wu H-H, Wu X, Pan K, Zhang Q (2020) Micro/nanostructured $TiNb_2O_7$-related electrode materials for high-performance electrochemical energy storage: recent advances and future prospects. J Mater Chem A 8:18425–18463. https://doi.org/10.1039/d0ta04209a

33. Griffith KJ, Seymour ID, Hope MA, Butala MM, Lamontagne LK, Preefer MB, Koçer CP, Henkelman G, Morris AJ, Cliffe MJ, Dutton SE, Grey CP (2019) Ionic and electronic conduction in $TiNb_2O_7$. J Am Chem Soc 141:16706–16725. https://doi.org/10.1021/jacs.9b06669

34. Cheng L-Q, He Y, Chen K, Ma Z, Liu R, Liu N, Deng Y (2022) Facile fabrication of a high performance $TiNb_2O_7$ anode for large-scale electrical energy storage. J Mater Chem A 10:17586–17592. https://doi.org/10.1039/D2TA03995H

35. Yang W, Bai C-J, Xiang W, Song Y, Xu C-L, Qiu L, He F-R, Zhang J, Sun Y, Liu Y, Zhong B-H, Wu Z-G, Guo X-D (2021) Dual-modified compact layer and superficial Ti doping for reinforced structural integrity and thermal stability of Ni-rich cathodes. ACS Appl Mater Interfaces 13:54997–55006. https://doi.org/10.1021/acsami.1c15920

36. Li S, Cao X, Schmidt CN, Xu Q, Uchaker E, Pei Y, Cao G (2016) $TiNb_2O_7$/graphene composites as high-rate anode materials for lithium/sodium ion batteries. J Mater Chem A 4:4242–4251. https://doi.org/10.1039/C5TA10510B

37. Liu W, Liu P, Mitlin D (2020) Review of emerging concepts in SEI analysis and artificial SEI membranes for lithium, sodium, and potassium metal battery anodes. Adv Energy Mater 10:2002297. https://doi.org/10.1002/aenm.202002297

38. Catti M, Pinus I, Knight K (2015) Lithium insertion properties of $Li_xTiNb_2O_7$ investigated by neutron diffraction and first-principles

modelling. J Solid State Chem 229:19–25. https://doi.org/10.1016/j.jssc.2015.05.011

39. Fei L, Xu Y, Wu X, Li Y, Xie P, Deng S, Smirnov S, Luo H (2013) SBA-15 confined synthesis of $TiNb_2O_7$ nanoparticles for lithium-ion batteries. Nanoscale 5:11102–11107. https://doi.org/10.1039/C3NR03594H

40. Yao W, Liu Y, Li D, Zhang Q, Zhong S, Cheng H, Yan Z (2020) Synergistically Enhanced electrochemical performance of Ni-rich cathode materials for lithium-ion batteries by K and Ti Co-modification. J Phys Chem C 124:2346–2356. https://doi.org/10.1021/acs.jpcc.9b10526

41. Hu J, Li W, Duan Y, Cui S, Song X, Liu Y, Zheng J, Lin Y, Pan F (2017) Single-Particle performances and properties of $LiFePO_4$ nanocrystals for Li-ion batteries. Adv Energy Mater 7:1601894. https://doi.org/10.1002/aenm.201601894